Dynamically Induced Symmetry Breaking and Out-of-Equilibrium Topology in a 1D Quantum System

G. H. Reid, Mingwu Lu, A. R. Fritsch, A. M. Piñeiro, and I. B. Spielman, Joint Quantum Institute, National Institute of Standards and Technology, and University of Maryland, Gaithersburg, Maryland 20899, USA

(Received 22 April 2022; accepted 8 August 2022; published 16 September 2022)

Nontrivial topology in lattices is characterized by invariants—such as the Zak phase for one-dimensional (1D) lattices—derived from wave functions covering the Brillouin zone. We realize the 1D bipartite Rice-Mele (RM) lattice using ultracold 87 Rb and focus on lattice configurations possessing various combinations of chiral, time-reversal, and particle-hole symmetries. We quench between configurations and use a form of quantum state tomography, enabled by diabatically tuning lattice parameters, to directly follow the time evolution of the Zak phase as well as a chiral winding number. The Zak phase evolves continuously; however, when chiral symmetry transiently appears in the out-of-equilibrium system, the chiral winding number becomes well defined and can take on any integer value. When quenching between two configurations obeying the same three symmetries, the Zak phase is time independent; we confirm the dynamically induced symmetry breaking predicted in [McGinley and Cooper, Phys. Rev. Lett. 121, 090401 (2018)] that chiral symmetry is periodically restored, at which times the winding number changes by ± 2 , yielding values that are not present in the native RM Hamiltonian.

DOI: 10.1103/PhysRevLett.129.123202

Topological invariants robustly classify gapped quantum systems in equilibrium. In addition to dimensionality, the presence or absence of symmetries determines the topological invariants that characterize them [1–3]. Thus, these invariants remain constant, provided that no gaps close and reopen and no symmetries are added or removed. One might expect the topology of dynamical quantum systems to be similarly robust; this expectation is untrue. We experimentally study the changing topology of ultracold atoms in a one-dimensional (1D) bipartite lattice in terms of the Zak phase [4] and chiral winding number. As predicted by Ref. [5], we find that these quantities can evolve in time depending on how symmetries change between the initial state and the evolution Hamiltonian.

Despite their relative simplicity, 1D bipartite lattices have nontrivial topology [6] characterized by the Zak phase

$$\phi_{\rm Z} = i \int_{\rm BZ} dq \langle \psi(q) | \partial_q | \psi(q) \rangle, \tag{1}$$

a Berry's phase [7] resulting from the distribution of crystal momentum states $|\psi(q)\rangle$ throughout the Brillouin zone (BZ). We implement a general approach for obtaining the Zak phase by measuring the wave function through a form of quantum state tomography [8] and directly evaluating Eq. (1). The Zak phase has been previously measured using a special-purpose interferometric technique with cold atoms [9], in photonic systems [10,11], and resonant circuits [12].

We employ a bipartite optical lattice [13,14] to realize the Rice-Mele (RM) Hamiltonian [15]

$$\hat{H}_{RM} = \sum_{j} [-(J'|j)\langle j| + J|j + 1\rangle\langle j|) \otimes |\downarrow\rangle\langle\uparrow| + \text{H.c.}$$

$$+ \Delta|j\rangle\langle j| \otimes \hat{\sigma}_{z}], \tag{2}$$

where j labels the unit cell; \uparrow and \downarrow identify sublattice sites that we associate with a pseudospin degree of freedom; and J and J' are the intercell and intracell tunneling strengths, respectively. For the special case of $\Delta=0$, the RM Hamiltonian reduces to the highly symmetric Su-Schrieffer-Heeger (SSH) Hamiltonian [16]. The SSH Hamiltonian obeys a chiral sublattice symmetry (CS) $\hat{S} \hat{H} \hat{S}^{\dagger} = -\hat{H}$ with $\hat{S} = \hat{\sigma}_z$, a particle-hole symmetry (PHS) $\hat{C} \hat{H}^* \hat{C}^{\dagger} = -\hat{H}$ with $\hat{C} = \hat{\sigma}_z$, as well as time-reversal symmetry (TRS) $\hat{T} \hat{H}^* T^{\dagger} = \hat{H}$ with $\hat{T} = \hat{T}$ [17]. As shown in Fig. 1(a), we label lattices with $\Delta=0$ and $J\gg J'$ as configuration I (topologically nontrivial with $\phi_Z=\pi$) and those with $\Delta=0$ and $J'\gg J$ as configuration II (topologically trivial with $\phi_Z=0$).

In the RM model (with only TRS), the Zak phase is real valued and defined mod 2π ; for the SSH model (with all three symmetries), the constraint on the Zak phase changes to $\phi_{\rm Z}/\pi=\nu$, defining an integer-valued winding number ν . Here, CS constrains the eigenstates of Eq. (2) to reside in the equatorial plane of the Bloch sphere, and the

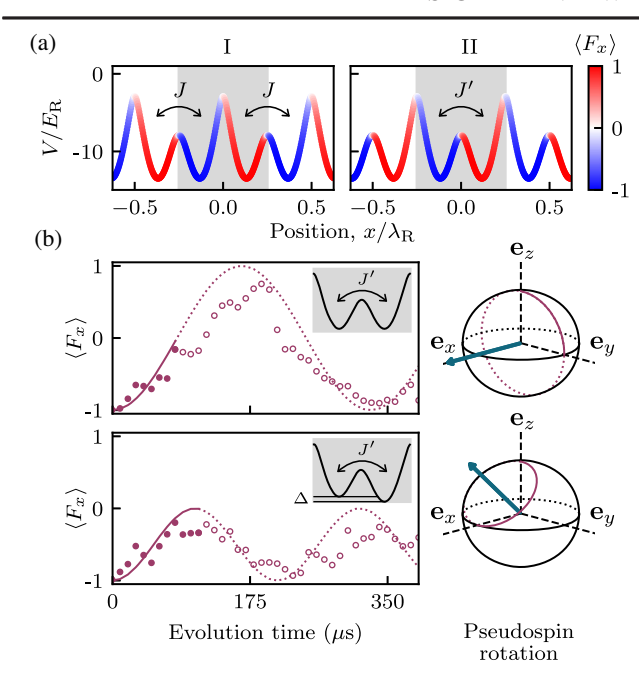


FIG. 1. (a) Adiabatic potentials colored according to the local magnetization for configurations I and II with the j=0 unit cell marked in gray, computed for $(\Omega_+=13.2E_R,\Omega_-=5.5E_R)$, $\Omega_{\rm rf}=3.5E_R)$. (b) Pseudospin evolution in the "y" and "x" readout lattices. The left panels plot $\langle \hat{F}_x \rangle (t)$ evolving according to the lattice pictured in its inset (symbols represent experiment; solid curves show theory); times up to the rotation time for the readout lattice are shown with solid symbols and curves, while evolution after this time is shown with open symbols or dotted curves. The right panels show the computed evolution on the Bloch sphere for these trajectories, along with the axis of rotation in blue.

topological invariant ν counts the number of times the state encircles the equator as q traverses the BZ [6,18,19].

We experimentally and numerically study initial states characterized by two different symmetries and evolve them according to the SSH Hamiltonian in both the trivial and topological configurations. When PHS and CS are absent in the initial state, ϕ_Z evolves in time, except when J=0 [20]. When no symmetries change, ϕ_Z is time independent; however, in agreement with Ref. [5], the time-evolving state periodically recovers CS at times where the winding number ν becomes well defined: dynamically induced symmetry breaking. Remarkably, we observe ν alternating either between -1 and +1 or between 0 and -2, even though the SSH model only allows winding numbers 0 and ± 1 .

Experimental system.—Our experiments begin with harmonically trapped ⁸⁷Rb Bose-Einstein condensates [BECs, with trap frequencies $(f_x, f_y, f_z) \approx (25, 150, 100)$ Hz] in the $|f=1, m_F=-1\rangle$ hyperfine state, which experience two "Raman" fields (generated by lasers with wavelength $\lambda_{\rm R} \approx 790$ nm and Rabi frequencies Ω_+ and Ω_-) and one radiofrequency (rf) magnetic field (with Rabi frequency $\Omega_{\rm rf}$ and phase $\phi_{\rm rf}$ with respect to the Raman fields), coupling the $|f=1, m_f=0, \pm 1\rangle$ hyperfine states. The single photon

recoil wave vector $k_{\rm R}=2\pi/\lambda_{\rm R}$ and energy $E_{\rm R}=\hbar^2k_{\rm R}^2/2m$ specify the natural momentum and energy scales of this system. This combination of Raman and rf fields approximates the RM Hamiltonian [21] derived from the adiabatic potentials in Fig. 1(a), with unit cell length $\lambda_{\rm R}/2$. In practice, $\phi_{\rm rf}$ controls the energy splitting Δ and selects the SSH configuration [21].

We load the BEC into the lattice in a three-step process. First, the rf and Raman fields ramp on in 2.5 ms, transferring the BEC to the lowest band of an initialization lattice. Second, we dephase the BEC to fill the BZ [21,23], and third, we switch to the final SSH configuration.

We measure the pseudospin resolved momentum distribution by combining momentum focusing time-of-flight (TOF) imaging [24] with a form of quantum state tomography. The \uparrow and \downarrow sites are highly polarized, with $\langle \hat{F}_x \rangle \approx \pm 1$, corresponding to atomic states $|m_x = \pm 1\rangle$ as indicated by the coloration in Fig. 1(a). Our default readout sequence begins by removing the coupling fields and applying an rf pulse to map eigenstates of \hat{F}_x to the standard \hat{F}_z measurement basis [21]. During the following TOF, a magnetic field gradient separates the hyperfine states by the Stern-Gerlach effect, yielding the momentum distribution of the $|\uparrow,\downarrow\rangle$ pseudospin states. Summing the populations separated by $2k_R$ yields the pseudospin resolved crystal momentum distribution, from which we obtain $\langle \hat{\sigma}_z(q) \rangle$.

We find $\langle \hat{\sigma}_x(q) \rangle$ and $\langle \hat{\sigma}_y(q) \rangle$ by evolving our system under one of two readout lattices depicted in Fig. 1(b) prior to this measurement sequence. The "y" readout lattice shown in (b) is described by a RM model with $J=\Delta=0$; unitary evolution under this lattice implements pseudospin rotations about $\hat{\sigma}_x$. Evolving for a $\pi/2$ time transforms $|y_\pm\rangle$ to $|\uparrow\downarrow\rangle$ (right). The "x" readout lattice in (b) uses $\Delta\approx J'$ and similarly transforms $|x_\pm\rangle$ to $|\uparrow\downarrow\rangle$ [21]. Combining these three complementary measurements allows us to reconstruct the pseudospin Bloch vector $\langle \hat{\boldsymbol{\sigma}}(q) \rangle \equiv \{\langle \hat{\sigma}_x(q) \rangle, \langle \hat{\sigma}_y(q) \rangle, \langle \hat{\sigma}_z(q) \rangle\}$. This readout scheme complements existing forms of Bloch state tomography in and out of equilibrium [25–28].

Quantum state tomography reconstructs the density operator from a set of expectation values, here $\langle \hat{\sigma}(q) \rangle$. In general, our measurement has imperfect contrast, reducing the purity of the reconstructed density operator. To compare with predicted pure states, we compute the pure state that most closely matches our experimental result by taking the principal eigenvector of the density operator, in the spirit of Ref. [29] [equivalent to normalizing $\langle \hat{\sigma}(q) \rangle$ [30]].

We validate our pseudospin measurement method by obtaining $\langle \hat{\sigma}(q) \rangle$ for ground band eigenstates in both configurations. The momentum-space Hamiltonian $\hat{H}(q) = -h(q) \cdot \hat{\sigma}$ is expressed in terms of a polarizing field

$$h(q) = \left[J' + J \cos\left(\frac{\pi q}{k_R}\right), J \sin\left(\frac{\pi q}{k_R}\right), \Delta \right]$$
 (3)

defining the axis along which the eigenstates are aligned. In limiting cases of configurations I and II, these axes are $[\cos(\pi q/k_{\rm R}),\sin(\pi q/k_{\rm R}),0]$ and [1,0,0], respectively.

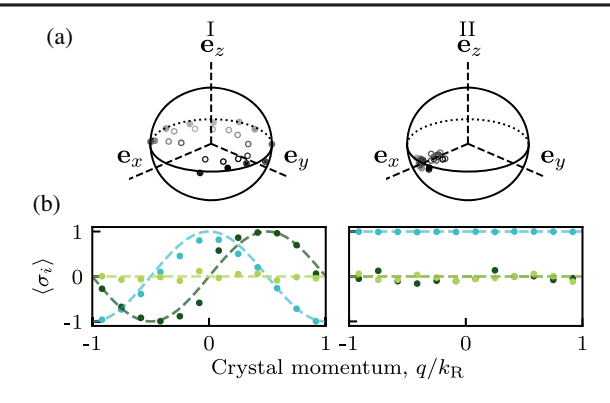


FIG. 2. Ground band pseudospin decomposition in SSH configurations I and II. (a) Pseudospin state for q values sampling the whole BZ plotted in the Bloch sphere. The raw measurements (open symbols) are impure (i.e., magnitude < 1); the solid symbols mark the nearest pure states on the surface of the Bloch sphere. For the eigenstates of configuration I, the vectors trace the equator of the Bloch sphere, while for configuration II, they are aligned along \mathbf{e}_x . (b) Pure-state expectation values of $\hat{\sigma}_x$, $\hat{\sigma}_y$, and $\hat{\sigma}_z$ shown as a function of q in light blue, dark green, and light green, plotted along with theory (dashed curves).

Figure 2 shows our observation of $\langle \hat{\sigma}(q) \rangle$ for configurations I (left) and II (right); diagrams in (a) render these data as points on the Bloch sphere, and the panels in (b) plot the components of $\langle \hat{\sigma}(q) \rangle$. Hollow symbols inside the Bloch sphere display our raw measurements, showing reduction purity from the combination of imperfect measurement and state preparation, while reconstructed states correspond to solid symbols [29]. For configuration I, the eigenstates encircle the equator of the Bloch sphere as q ranges from $-k_R$ to $+k_R$, giving a Zak phase $\phi_Z = \pi$. By contrast, in configuration II, the eigenstates are q independent, giving $\phi_Z = 0$.

Following Ref. [31], we experimentally obtain ϕ_Z from discretely sampled q. In good agreement with the theory, this gives $0.99(3)\pi$ and $-0.0005(1)\pi$ for configurations I and II, respectively [32].

Topology out of equilibrium.—Having measured the Zak phase of eigenstates of the SSH model, we turn to the dynamics of initial states characterized by different symmetries evolving under the SSH Hamiltonian, which respects all three symmetries (CS, PHS, and TRS).

We first focus on the q-independent initial state $|\psi(q)\rangle = |\downarrow\rangle$, the ground state of the $\Delta\gg(J,J')$ RM Hamiltonian that only retains TRS. This initial state is prepared by adiabatically loading into a maximally imbalanced initialization lattice with $\Delta\approx 5E_{\rm R}$ and $J=J'\approx 0.1E_{\rm R}$. We initialize evolution by abruptly switching to a maximally dimerized lattice with $\Delta=0$ in either configuration I or II.

In both configurations, chiral symmetry implies that $\mathbf{h}(q)$ is in the \mathbf{e}_x - \mathbf{e}_y plane, and owing to the nearly flat bands of the highly dimerized SSH Hamiltonian, $|\mathbf{h}(q)|$ is almost constant. As a result, $\langle \hat{\sigma}_z \rangle$ exhibits nearly

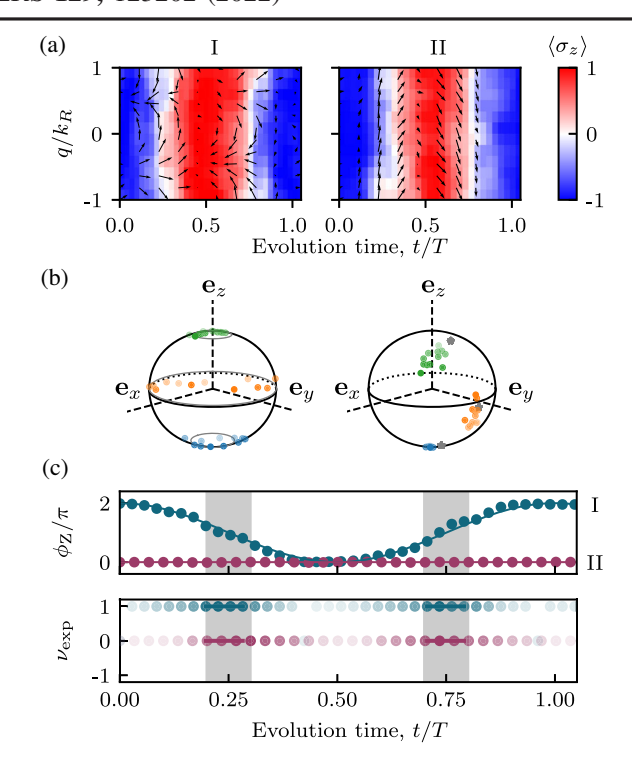


FIG. 3. Momentum resolved pseudospin evolution in SSH configurations I and II. Model parameters are $J=0.395(2)E_{\rm R}$, $J'=0.012(2)E_{\rm R}$ for configuration I and $J=0.038(3)E_{\rm R}$, $J'=0.379(2)E_{\rm R}$ for configuration II. (a) Reconstructed Bloch vectors. Colors represent $\langle \hat{\sigma}_z(q) \rangle$ while black arrows denote $(\langle \hat{\sigma}_x(q) \rangle, \langle \hat{\sigma}_y(q) \rangle)$. The data are filtered in crystal momentum and time (with root-mean-square Gaussian widths $k_{\rm R}/8$ and $10~\mu \rm s$). (b) Corresponding points on the Bloch sphere for evolution times of (0.05, 0.25, 0.45)~T. (c) Zak phase and winding number for configurations I (teal) and II (magenta). The transparency indicates the extent to which the measured state breaks CS, and the gray boxes surround the times when CS is predicted to be recovered.

q-independent full contrast oscillations for the $|\downarrow\rangle$ initial state as shown in Fig. 3(a). The $\langle \hat{\sigma}_{x,y} \rangle$ components (black arrows) evolve in a q-dependent way in configuration I but are q independent in configuration II.

In configuration I, each q state orbits about a different axis in the \mathbf{e}_x - \mathbf{e}_y plane, causing $\langle \hat{\boldsymbol{\sigma}}(q) \rangle$ to first spread and then encircle the Bloch sphere, before ascending to converge at $|\uparrow\rangle$. The corresponding evolution of the Zak phase [teal points in Fig. 3(c)] starts at $2\pi = (0 \mod 2\pi)$ and reaches π when $\langle \hat{\boldsymbol{\sigma}}(q) \rangle$ reaches the equator. When $\langle \hat{\boldsymbol{\sigma}}(q) \rangle = \mathbf{e}_z$, the Zak phase reaches its extremal value of 0. The state continues to evolve, returning to the initial configuration at $T \approx 360 \ \mu \text{s}$.

In configuration II, $\mathbf{h}(q) = [J', 0, 0]$; as a result, $\langle \hat{\boldsymbol{\sigma}}(q) \rangle$ orbits around \mathbf{e}_x , independent of q, starting from the $-\mathbf{e}_z$ pole and reaching the $+\mathbf{e}_z$ pole via \mathbf{e}_y and returning to $-\mathbf{e}_z$. The derivative in Eq. (1) implies $\phi_Z = 0$ at all times, in agreement with our observations [magenta points in Fig. 3(c)]. More generally, the SSH Hamiltonian (with

 $J, J' \neq 0$) has q-dependent evolution, making the Zak phase time dependent except when J=0. In both configurations, the time-evolving state is always an eigenstate of some RM Hamiltonian in the initial configuration, but with time-dependent Δ and complex tunneling. For most of the evolution, the state is described by a RM model violating all symmetries (nontopological symmetry class A, see Ref. [3]). Twice every oscillation, $\langle \hat{\sigma}(q) \rangle$ aligns along e_z, at which times the state obeys TRS but violates CS (nontopological symmetry class AI). Similarly, $\langle \hat{\sigma}(q) \rangle$ lies on the equator twice per oscillation, and the system becomes an eigenstate of the SSH model with complex tunneling phase $\phi = \pm \pi/2$, thereby recovering CS but violating TRS (topological symmetry class AIII). The recovered chiral symmetry makes the winding number well defined, with $\nu = 1$ in configuration I and $\nu = 0$ in configuration II.

Because all experimental data have some contribution along \mathbf{e}_z and therefore violate CS to some degree, we project the measurements onto the \mathbf{e}_x - \mathbf{e}_y plane, enforcing CS, before computing an integer-valued winding number $\nu_{\rm exp}$ [bottom panel of Fig. 3(c)]. The intensity of each symbol marks the projection of the reconstructed state onto the \mathbf{e}_x - \mathbf{e}_y plane, so bold symbols mark states with little violation of CS. The vertical gray bands mark the regions within 10% of T/4 + nT/2, when CS is expected to be recovered. Note that $\nu_{\rm exp}$ is defined at all times but should only be compared to ν when CS is recovered. We see that within the gray bands, the CS is maximally restored (bold symbols), and we confirm $\nu_{\rm exp} = \nu$ for these times.

Dynamically induced symmetry breaking.—We conclude by investigating cases where the initial state and evolution Hamiltonian respect all three symmetries—TRS, PHS, and CS—by preparing eigenstates of the fully dimerized SSH Hamiltonian and then evolving under the opposite SSH configuration. As one might expect, the Zak phase is predicted to be constant at all times; however, CS is lost during much of the evolution, and when it is recovered, ν can take on values that are not present in the SSH Hamiltonian, confirming a counterintuitive prediction of Ref. [5].

As before, when the system evolves in configuration I, the state for each q value orbits a different axis in the \mathbf{e}_x - \mathbf{e}_y plane, giving the distributions in Fig. 4(a) (left panel). In this case, the initial state, a configuration II eigenstate, has $\langle \hat{\sigma}(q) \rangle$ aligned along \mathbf{e}_x for all q. Figure 4(b) (left panel) shows that the time evolution of $\langle \hat{\sigma}(q) \rangle$ traces out a figure-8 shape consisting of symmetric loops in the upper and lower hemispheres of the Bloch sphere. Ideally, the Zak phase is time independent since the two loops enclose equal areas but are traced in opposite directions as a function of q, giving equal but opposite contributions to Eq. (1). The data in Fig. 4(c) are in qualitative agreement with this prediction. Despite this, the topology of the state changes when the state recovers CS every $T/2 = \pi/(2J) \approx 160~\mu \text{s}$ when

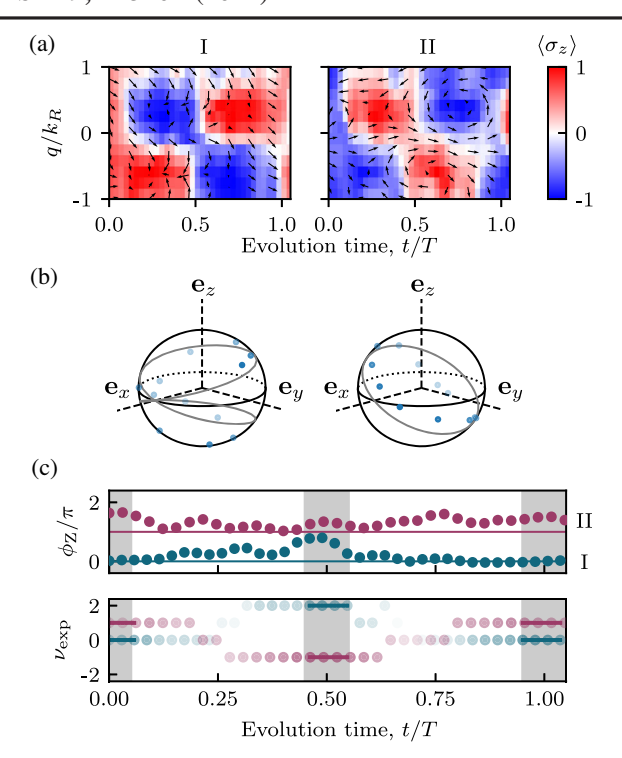


FIG. 4. Momentum resolved pseudospin evolution in SSH configurations I and II, using initial states of the opposite configuration. Model parameters are $J=0.408(3)E_{\rm R}$, $J'=0.003(5)E_{\rm R}$ for configuration I and $J=0.009(5)E_{\rm R}$, $J'=0.446(3)E_{\rm R}$ for configuration II. All panels are plotted as in Fig. 3. (a) Individual expectation values $\langle \hat{\sigma}_x \rangle$, $\langle \hat{\sigma}_y \rangle$, and $\langle \hat{\sigma}_z \rangle$. (As before, the data are filtered with root-mean-square Gaussian widths $k_{\rm R}/8$ and $10~\mu{\rm s.}$) (b) Bloch state rendering at t=0.40T. (c) Zak phase and winding number for configurations I (teal) and II (magenta).

 ν alternates between 0 and 2 [Fig. 4(c)], which is not possible for a SSH model eigenstate.

Figure 4(a) (right panel) shows evolution under configuration II, again resulting from a q-independent rotation around \mathbf{e}_x . In this case, the initial state is a configuration I eigenstate where $\langle \hat{\sigma}(q) \rangle$ fully encircles the equator of the Bloch sphere. As time evolves, $\langle \hat{\sigma}(q) \rangle$ describes a great circle rotated by an angle 2J't about \mathbf{e}_x as shown in Fig. 4(b) (right panel). Since the circle always encloses half the area of the Bloch sphere, we expect $\phi_Z = \pi$ for all time. As in the previous case, the state periodically recovers CS when it returns to the equator, at which times the winding number alternates between $\nu = +1$ and -1.

The top panel of Fig. 4(c) plots the time-evolving Zak phase in configurations I and II in teal and magenta, respectively. Both of these fluctuate near the expected constant value; we attribute these fluctuations to imperfections in state preparation, the evolution Hamiltonian, and our readout process. As in Fig. 3, the gray bands mark the expected times when CS is restored, and in agreement with our model, $\nu_{\rm exp}$ oscillates between 0 and 2 for configuration II and between +1 and -1 for configuration II. This is

possible because the Zak phase is defined modulo 2π , allowing for ν to change by multiples of 2 at constant ϕ_Z . We note that while ϕ_Z can be heavily affected by noise and imperfections as seen in Fig. 4(c), $\nu_{\rm exp}$ is more robust, deviating from the prediction only when the noise is comparable in strength to the projected measurements.

Discussion and outlook.—We presented paradigmatic examples of how the topology of a quantum system can change during out-of-equilibrium evolution. From a macroscopic perspective, the out-of-equilibrium evolution of the Zak phase is associated with a current between unit cells and the resulting change in polarization [5]. In configuration II, there is no current between unit cells, and the Zak phase must be constant; in configuration I, the probability amplitude oscillates between sites in adjacent unit cells, and the Zak phase changes. The associated physical displacement was directly observed in Ref. [14] while observing Floquet topological invariants [33].

At times when $\nu=2$, the system approaches an eigenstate of an extended SSH model where next-nearest-neighbor tunneling dominates [34]. This marks the ability of unitary evolution under relatively simple Hamiltonians to dynamically prepare eigenstates of experimentally inaccessible models. A natural extension of this Letter is dynamical symmetry breaking and recovery for strongly correlated systems: When do similar concepts apply to interacting systems, and what otherwise inaccessible eigenstates can be realized?

We thank M. McGinley and N. R. Cooper for helpful discussions, as well as N. Pomata and M. Doris for carefully reading our manuscript. This work was partially supported by the National Institute of Standards and Technology, and the National Science Foundation through the Physics Frontier Center at the Joint Quantum Institute (Grant No. PHY-1430094), and the Quantum Leap Challenge Institute for Robust Quantum Simulation (Grant No. OMA-2120757).

- *ian.spielman@nist.gov
- [1] A. P. Schnyder, S. Ryu, A. Furusaki, and A. W. W. Ludwig, Classification of topological insulators and superconductors in three spatial dimensions, Phys. Rev. B **78**, 195125 (2008).
- [2] A. Kitaev, Periodic table for topological insulators and superconductors, in AIP Conference Proceedings (American Institute of Physics, New York, 2009), Vol. 1134, pp. 22–30.
- [3] C.-K. Chiu, J. C. Y. Teo, A. P. Schnyder, and S. Ryu, Classification of topological quantum matter with symmetries, Rev. Mod. Phys. 88, 035005 (2016).
- [4] J. Zak, Berry's Phase for Energy Bands in Solids, Phys. Rev. Lett. **62**, 2747 (1989).
- [5] M. McGinley and N. R. Cooper, Topology of One-Dimensional Quantum Systems Out of Equilibrium, Phys. Rev. Lett. 121, 090401 (2018).
- [6] J. K. Asbóth, L. Oroszlány, and A. Pályi, A short course on topological insulators, Lect. Notes Phys. 919, 166 (2016).

- [7] M. V. Berry, Quantal phase factors accompanying adiabatic changes, Proc. R. Soc. A 392, 45 (1984).
- [8] E. Alba, X. Fernandez-Gonzalvo, J. Mur-Petit, J. K. Pachos, and J. J. García-Ripoll, Seeing Topological Order in Timeof-Flight Measurements, Phys. Rev. Lett. 107, 235301 (2011).
- [9] M. Atala, M. Aidelsburger, J. T. Barreiro, D. Abanin, T. Kitagawa, E. Demler, and I. Bloch, Direct measurement of the Zak phase in topological Bloch bands, Nat. Phys. 9, 795 (2013).
- [10] Q. Wang, M. Xiao, H. Liu, S. Zhu, and C. T. Chan, Measurement of the Zak phase of photonic bands through the interface states of a metasurface/photonic crystal, Phys. Rev. B **93**, 041415(R) (2016).
- [11] F. Cardano, A. D'Errico, A. Dauphin, M. Maffei, B. Piccirillo, C. de Lisio, G. De Filippis, V. Cataudella, E. Santamato, L. Marrucci *et al.*, Detection of Zak phases and topological invariants in a chiral quantum walk of twisted photons, Nat. Commun. 8, 15516 (2017).
- [12] T. Goren, K. Plekhanov, F. Appas, and K. Le Hur, Topological Zak phase in strongly coupled LC circuits, Phys. Rev. B 97, 041106(R) (2018).
- [13] H.-I. Lu, M. Schemmer, L. M. Aycock, D. Genkina, S. Sugawa, and I. B. Spielman, Geometrical Pumping with a Bose-Einstein Condensate, Phys. Rev. Lett. 116, 200402 (2016).
- [14] M. Lu, G. H. Reid, A. R. Fritsch, A. M. Piñeiro, and I. B. Spielman, Floquet Engineering Topological Dirac Bands, Phys. Rev. Lett. 129, 040402 (2022).
- [15] M. J. Rice and E. J. Mele, Elementary Excitations of a Linearly Conjugated Diatomic Polymer, Phys. Rev. Lett. 49, 1455 (1982).
- [16] W. P. Su, J. R. Schrieffer, and A. J. Heeger, Solitons in Polyacetylene, Phys. Rev. Lett. 42, 1698 (1979).
- [17] Our expressions for the symmetry operations are the unitary part of the complete symmetry operator, where complex conjugation implicitly expresses the antiunitary contribution.
- [18] N. R. Cooper, J. Dalibard, and I. B. Spielman, Topological bands for ultracold atoms, Rev. Mod. Phys. **91**, 015005 (2019).
- [19] Although a winding number can be defined for any path that encircles \mathbf{e}_z (zero, one, or many times), it is only a topological invariant when the path resides on the equator of the Bloch sphere.
- [20] As discussed in Ref. [21], when TRS and PHS are absent in the initial state (but CS is present), ϕ_Z can also evolve in time.
- [21] See Supplemental Material at http://link.aps.org/supplemental/10.1103/PhysRevLett.129.123202 for further details of our experiment and pseudospin readout method and a complementary symmetry breaking experiment, which includes Ref. [22].
- [22] G. Juzeliūnas and I. B. Spielman, Flux lattices reformulated, New J. Phys. **14**, 123022 (2012).
- [23] A. M. Piñeiro, D. Genkina, M. Lu, and I. B. Spielman, Sauter–Schwinger effect with a quantum gas, New J. Phys. **21**, 083035 (2019).
- [24] A. H. van Amerongen, J. J. P. van Es, P. Wicke, K. V. Kheruntsyan, and N. J. van Druten, Yang-Yang Thermodynamics on an Atom Chip, Phys. Rev. Lett. **100**, 090402 (2008).

- [25] P. Hauke, M. Lewenstein, and A. Eckardt, Tomography of Band Insulators from Quench Dynamics, Phys. Rev. Lett. 113, 045303 (2014).
- [26] T. Li, L. Duca, M. Reitter, F. Grusdt, E. Demler, M. Endres, M. Schleier-Smith, I. Bloch, and U. Schneider, Bloch state tomography using Wilson lines, Science 352, 1094 (2016).
- [27] N. Fläschner, B. Rem, M. Tarnowski, D. Vogel, D.-S. Lühmann, K. Sengstock, and C. Weitenberg, Experimental reconstruction of the Berry curvature in a Floquet Bloch band, Science 352, 1091 (2016).
- [28] N. Fläschner, D. Vogel, M. Tarnowski, B. Rem, D.-S. Lühmann, M. Heyl, J. Budich, L. Mathey, K. Sengstock, and C. Weitenberg, Observation of dynamical vortices after quenches in a system with topology, Nat. Phys. 14, 265 (2018).
- [29] S. Diehl, E. Rico, M. A. Baranov, and P. Zoller, Topology by dissipation in atomic quantum wires, Nat. Phys. 7, 971 (2011).

- [30] This process leaves the overall phase undefined. The choice of phase can be viewed as a momentum space gauge transformation which affects no observables but may introduce an offset to the calculated Zak phase.
- [31] T. Fukui, Y. Hatsugai, and H. Suzuki, Chern numbers in discretized Brillouin zone: Efficient method of computing (spin) Hall conductances, J. Phys. Soc. Jpn. **74**, 1674 (2005).
- [32] The stated uncertainties are the sample standard deviation of the Zak phase calculated individually from about 30 separate measurements.
- [33] T. Kitagawa, E. Berg, M. Rudner, and E. Demler, Topological characterization of periodically driven quantum systems, Phys. Rev. B **82**, 235114 (2010).
- [34] H.-C. Hsu and T.-W. Chen, Topological Anderson insulating phases in the long-range Su-Schrieffer-Heeger model, Phys. Rev. B 102, 205425 (2020).